Supporting Information

Tuning Spontaneous Polarization and Optical Absorption by Intercalating Sr-Cl-Layers in Organic-Inorganic Halide Perovskite $CH_3NH_3PbI_3$ Thin Films

Xiao-dong Yang[a, b], *Cheng Lu*[a, b], *Xin-xin Wang*[a, b], *Bao-lin Wang*[c], *Gui-xian Ge*[a, b, d], *Guang-hou Wang*[a, b] *and Jian-guo Wan*[*, a, b]

[a]National Laboratory of Solid State Microstructures and Department of Physics, Nanjing University, Nanjing 210093, P. R. China. Email: wanjg@nju.edu.cn

[b]Collaborative Innovation Center of Advanced Microstructures, Nanjing University, Nanjing 210093, P. R. China

[c]College of Physical Science and Technology, Nanjing Normal University, Nanjing 210023, P. R. China

[d]Key Laboratory of Ecophysics and Department of Physics, College of Science, Shihezi University, Xinjiang 832003, P. R. China

Corresponding Author

*Email: wanjg@nju.edu.cn

Section S1. The computational details of HSE06+SOC method on perovskite

The HSE+SOC method is performed by using HSE06 hybrid functionals, where the long-ranged part of exchange interaction is substituted by the corresponding part of the PBE density functional. In this exchange-correlation energy functional, the short-ranged part of the electron-electron interaction of the non-local Fock exchange energy is 34%, short-ranged part of the exchange interactions of PBE density functional counterpart 66% and long-ranged exchange parts of PBE density functional and correlation parts of the PBE density functional are both 100%, respectively.

To verify the reliability of these parameters of HSE06+SOC method, we contrasted the band-gaps of bulk $CH_3NH_3PbI_3$ with different methods in Table S1. The values without citation at superscript were calculated by ourselves in this work. As shown in Table S1, our results are in accordance with others' calculations. Therefore, HSE06+SOC calculation is reasonable for the materials investigated and adequate to provide an accurate band-gap.

Table S1. Band-gaps calculated in this work by using various theory methods for bulk $MAPbI_3$.

	PBE	**SOC**	**HSE06+SOC**	**SOC+GW**	**Exp**
O-phase	1.70[1]	0.7953, 0.60[1]	1.7004	1.69[1]	1.64[2]
T-phase	1.70[3]	0.8141,0.75[3]	1.7056	1.67[4]	1.60[5]

Section S2. The crystal structures and electronic properties of bulk perovskites

Here we consider two common crystal phases (see Figure S1), i.e., orthorhombic phase and tetragonal phase (labeled as O-phase and T-phase, respectively). The calculated band structures and density of states (DOSs) for the O- and T-phases of the $MAPbI_3$ suggest that the electronic structures in O-phase have a strong resemblance to those in T-phases of both $MAPbI_3$. This phenomenon not only exists in $MAPbI_3$, but also in the two phases of $MASrI_3$. The $MASrI_3$ in O- and T-phases both have the direct band-gap with gap of ~3.9eV at the Γ point, which is in accordance with the

previously reported theoretical studies[6-8]. Such a result suggests that the electronic structures in O-phase have a strong resemblance to those in T-phases of both $MAPbI_3$ and $MASrI_3$. Thus, the electronic structures discussed in this letter will focus on the O-phases as the representative.

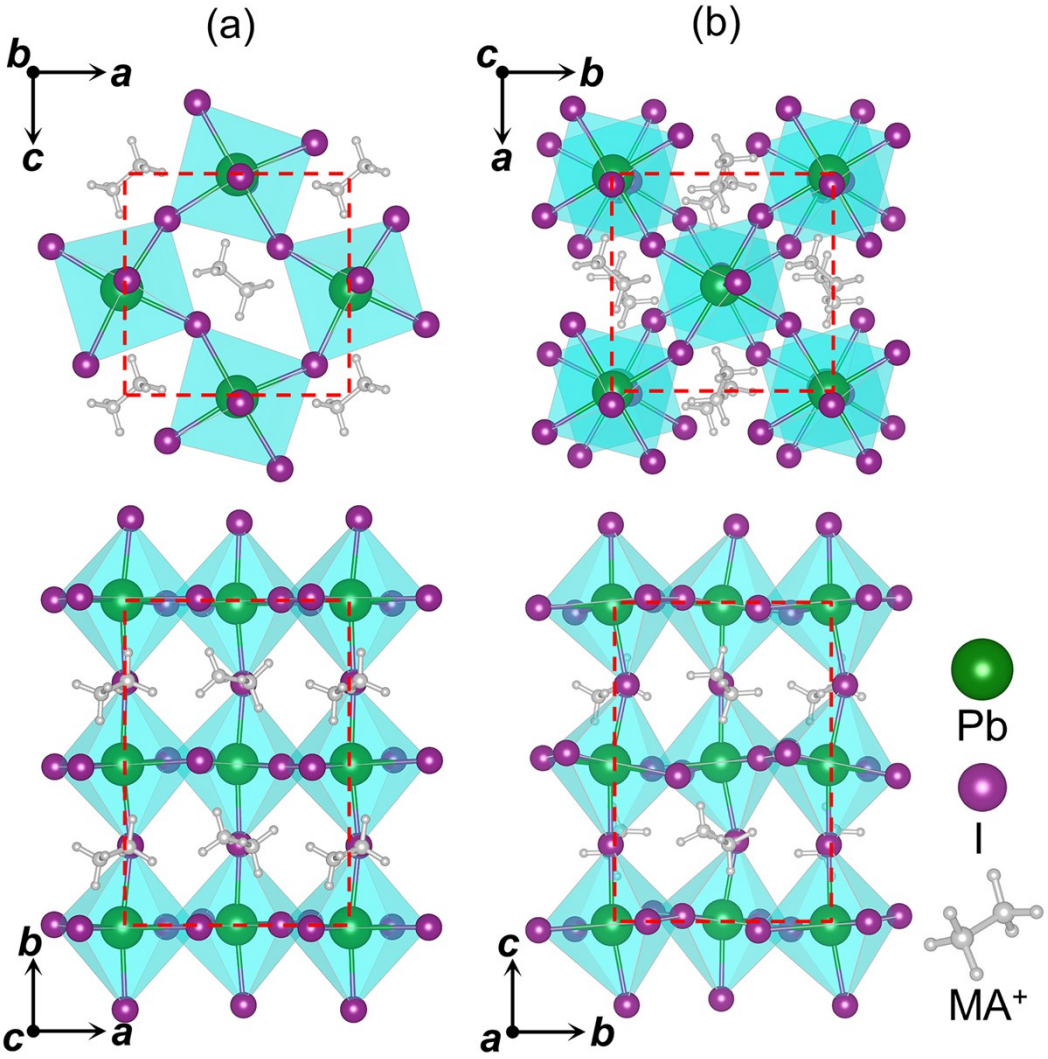

Figure S1. Crystal structures of (a) orthorhombic (O-) and (b) tetragonal (T-) phases of $MAPbI_3$. The upper and lower panels represent [001] and [100] crystallographic directions, respectively. The red dash lines denote the range of unit cell of bulk perovskites.

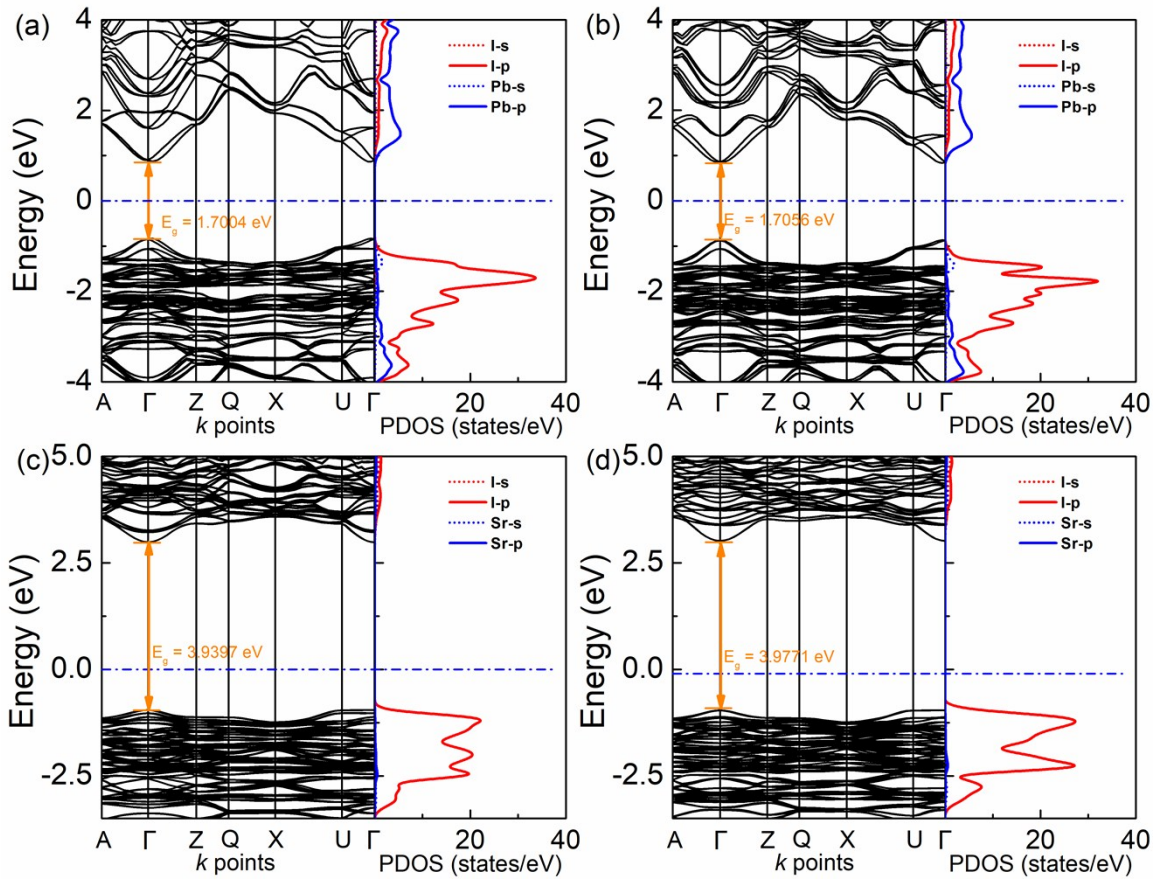

Figure S2. Calculated band structures and PDOSs for (a) O-phase of $MAPbI_3$, (b) T-phase of $MAPbI_3$, (c) O-phase of $MASrI_3$ and (d) T-phase of $MASrI_3$. The position of Fermi level is set to energy zero.

Section S3. The surface stabilities of $MAPbI_3$, $MASrI_3$ and $MASrCl_3$ thin films

In order to investigate the stability of $MAPbI_3$ surfaces with different terminations, relative surface energies (γ_s) for each surface are calculated by the following formulas:

$$\gamma_{vacant} = (E_T - n_v E_{MAPbI_3})/2A \quad \text{(S1)}$$

$$\gamma_s = \gamma_{vacant} + \left[\Delta E_T - \Delta n_{MAI}\mu_{MAI} - \Delta n_{PbI_2}\mu_{PbI_2}\right]/2A \quad \text{(S2)}$$

The surface energy of vacant terminated surface γ_{vacant} is obtained by eq S1, where E_T is the total energy of vacant terminated surface and E_{MAPbI_3} is the total energy/f.u. of $MAPbI_3$ in orthorhombic bulk. A is the area of vacant terminated surface and n_v is the number of $MAPbI_3$ in vacant terminated surface. Eq S2 indicates

that all the surface energies γ_s are calculated by taking the surface energy of vacant terminated surface as a reference because the stoichiometric ratio of vacant terminated surface is the same as that of bulk perovskite. ΔE_T is the total-energy between a given surface and the vacant terminated surface. The chemical potentials of the most stable reactants MAI and PbI_2, i.e., μ_{MAI} and μ_{PbI_2}, are considered to describe different chemical composition conditions because $MAPbI_3$ thin films have been successfully synthesized by using MAI, PbI_2 and other adducts[9, 10]. The allowed values of μ_{MAI} and μ_{PbI_2} are constrained by $\mu_{MAI} + \mu_{PbI_2} = E_{MAPbI_3}$ and the value of μ_{MAI} is in the range of $\mu_{MAI(bulk)} - \Delta H_f \leqslant \mu_{MAI} \leqslant \mu_{MAI(bulk)}$. The upper (lower) limit of μ_{MAI} corresponds to the MAI-rich (PbI_2-rich) condition and ΔH_f is the heat formation of orthorhombic bulk perovskite. The calculated ΔH_f of O-phase bulk $MAPbI_3$ is 0.2673 eV. Δn_{MAI} (Δn_{PbI_2}) is the difference between the number of MAI (PbI_2) in the given surface and the vacant terminated surface.

Similarly, we also investigate the stability of $MASrI_3$ and $MASrCl_3$ surfaces with different terminations, relative surface energies (γ_s) for each surface are calculated by the following formulas:

$$\gamma_{vacant} = (E_T - n_v E_{MASrI_3})/2A \quad \text{(S3)}$$

$$\gamma_s = \gamma_{vacant} + \left[\Delta E_T - \Delta n_{MAI}\mu_{MAI} - \Delta n_{SrI_2}\mu_{SrI_2}\right]/2A \quad \text{(S4)}$$

and

$$\gamma_{vacant} = (E_T - n_v E_{MASrCl_3})/2A \quad \text{(S5)}$$

$$\gamma_s = \gamma_{vacant} + \left[\Delta E_T - \Delta n_{MACl}\mu_{MACl} - \Delta n_{SrCl_2}\mu_{SrCl_2}\right]/2A \quad \text{(S6)}$$

The calculated ΔH_f of O-phase bulk $MASrI_3$ and $MASrCl_3$ are 0.2670 eV and 0.1124 eV, respectively.

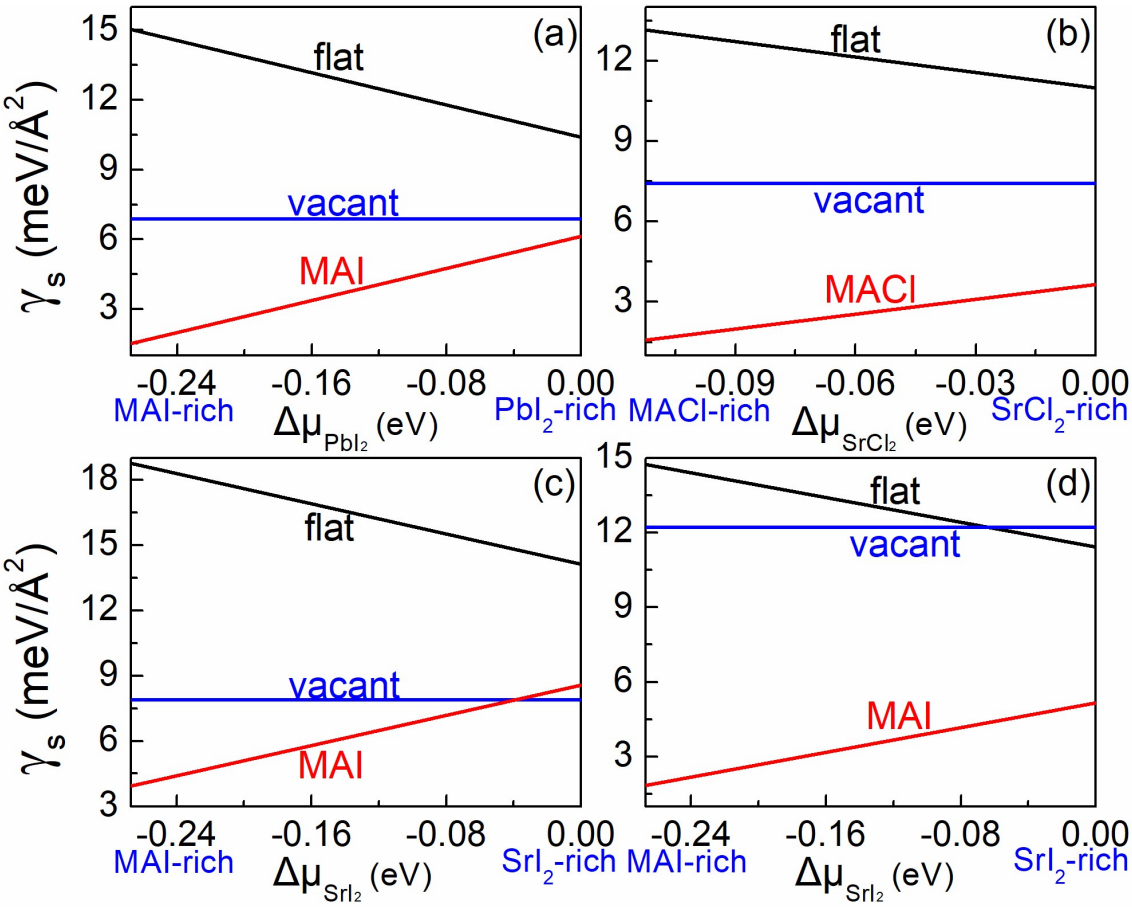

Figure S3. The surface energies of (a) {100} facets of $MAPbI_3$, (b) {100} facets of $MASrCl_3$, (c) {100} facets of $MASrI_3$ and (d) {110} facets of $MASrI_3$ with three types of surface terminations in different chemical potential conditions.

All the perovskites with the MA-halogen terminated surface are the most stable configuration in a large range of chemical potential, as shown in Figure S3. It is noted that in the case of {100} facets of $MASrI_3$, vacant terminated surface becomes the most stable surface structure in the SrI_2-rich environment, as shown in Figure S3(c). However, the quantity of MAI and SrI_2 are approximately equal to each other when $MASrI_3$ is synthesized in experiment. Therefore, compared to MAI terminated surfaces, flat and vacant terminated surfaces are still metastable.

Section S4. The surface effect on charge distributions of perovskite

Here we determine the band structures and charge-density distributions of

perovskites with {100} surfaces, as shown in Figure S4. The electrons and holes are located on the surfaces of pristine MPI, which is just like what occurs in {110} pristine MPI, as shown in Figure S4(a). This phenomenon is detrimental to applications in photoelectric devices because of the low carrier diffusion length and lifetime.

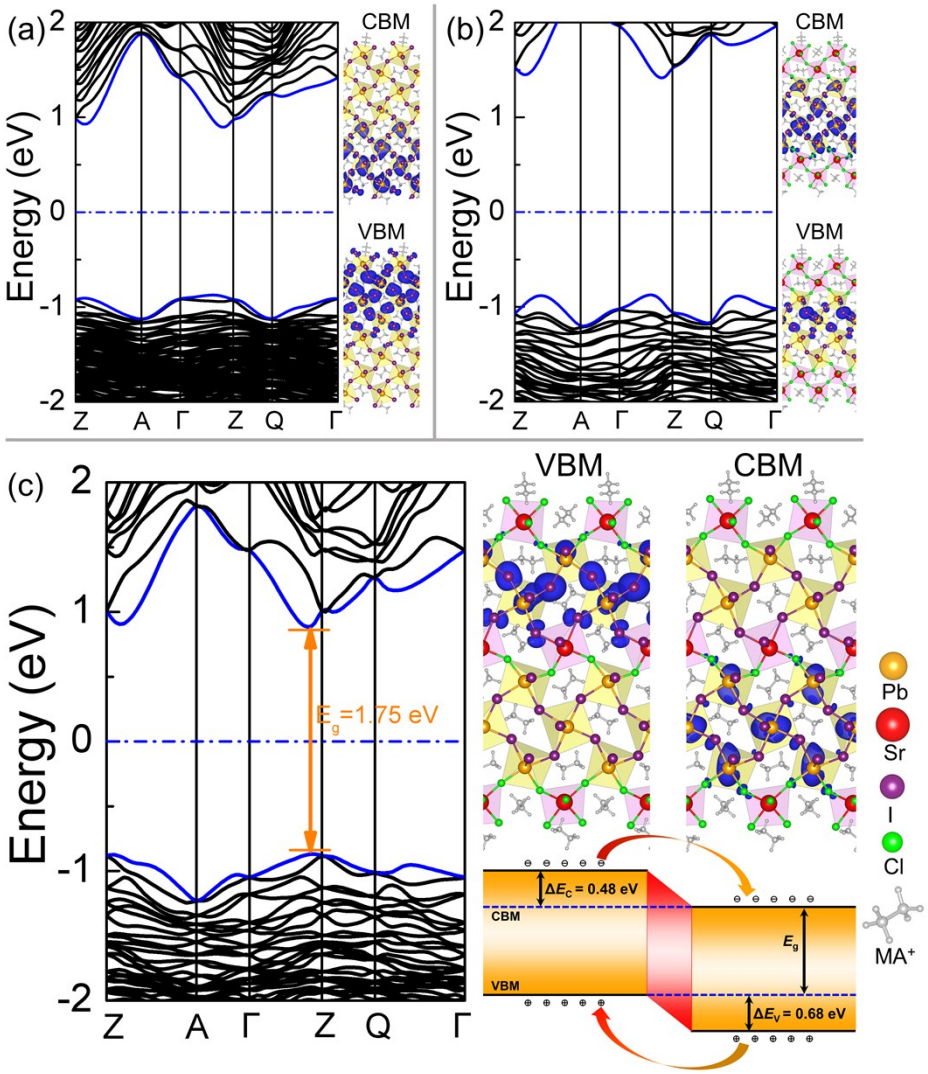

Figure S4. Band structures (left panel) and charge-density distributions of band-edge states (right panel) of layered (a) traditional MPI, (b) 1-0-1 type MPI and (c) 1-1-1 type MPI structures with {100} facets. The charge-density distributions correspond to the bands emphasized by blue. The position of Fermi level is set to energy zero.

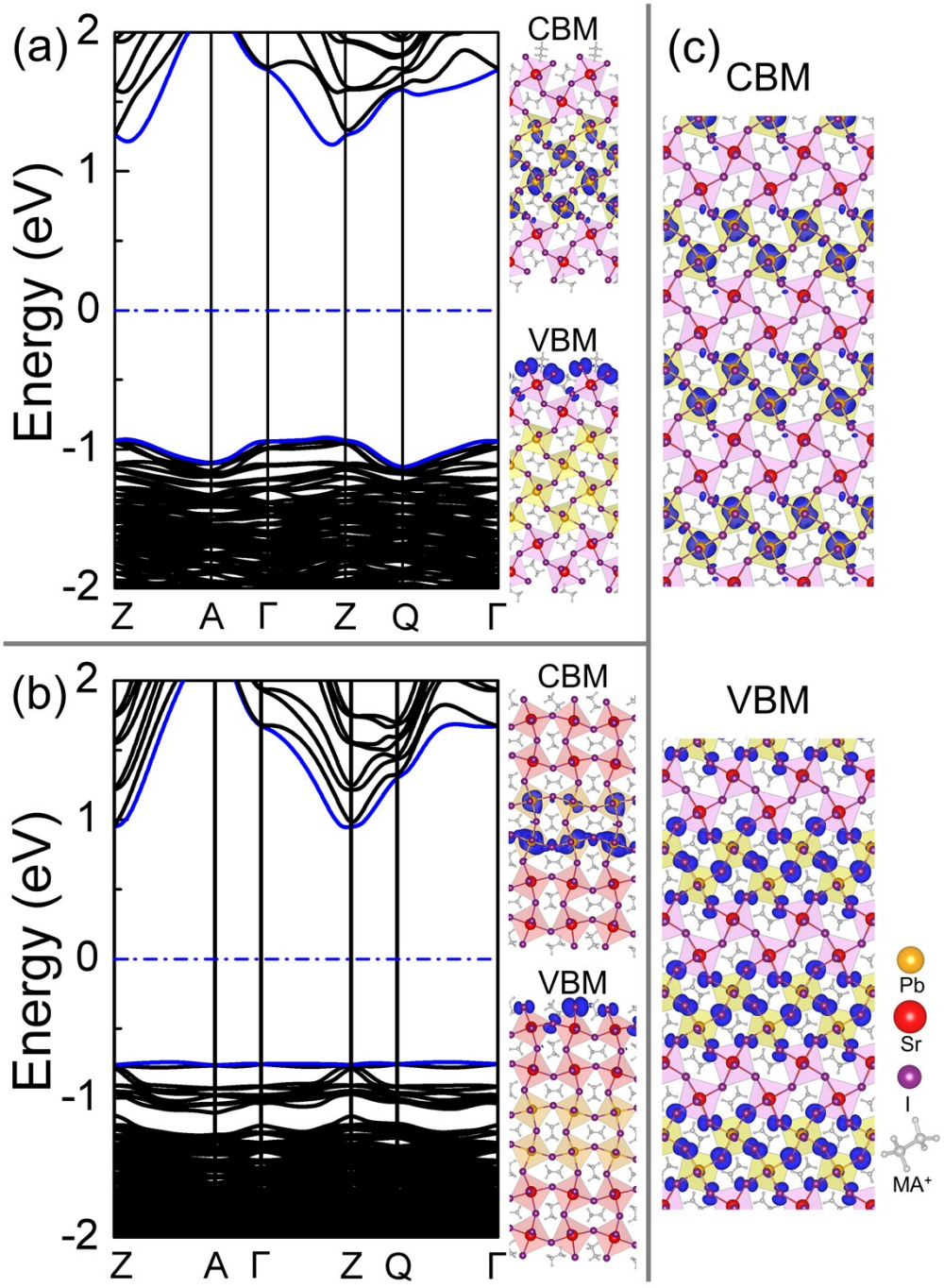

Figure S5. Band structures (left panel) and charge-density distributions of band-edge states (right panel) of $MASrI_3/MAPbI_3/MASrI_3$ film with (a) {100} and (b) {110} surfaces. The charge-density distributions correspond to the bands emphasized by blue. The position of Fermi level is set to energy zero. (c) The charge-density distributions of band-edge states in $MAPbI_3/MASrI_3$ superlattice.

To gain a deep insight into the surface effect on electronic properties of perovskite thin films, the electronic structures of $MASrI_3/MAPbI_3/MASrI_3$ sandwich configuration and $MAPbI_3/MASrI_3$ superlattice are considered (see Figure S5). Figure

S5(a) and (b) show that the electrons at CBM (conduction band minimum) are both distributed in the region of $MAPbI_3$, while the holes at VBM still accumulate at the surface of perovskite. This is because the conduct band (CB) of perovskite is mainly dominated by metal ions while valence band (VB) is determined by halogen atoms. Therefore, as strontium atoms doped into $MAPbI_3$, electrons at CBM will transfer to the $MAPbI_3$ region where the band-gap is much smaller than that of $MASrI_3$, while the holes at VBM keep on accumulating around iodine atoms at the surface. Thus, the surface states remain at the band-edge of $MASrI_3/MAPbI_3/MASrI_3$. As a reference, the charge-density distributions of CBM and VBM in $MAPbI_3/MASrI_3$ superlattice are plotted in Figure S5(c) as a contrast with those of perovskite thin films. The $MAPbI_3$ and $MASrI_3$ layers stack along the [001] direction in $MAPbI_3/MASrI_3$ superlattice, which has the similar configure to that of the $MASrI_3/MAPbI_3/MASrI_3$ sandwich structure with {100} surfaces. However, the difference is that the $MAPbI_3/MASrI_3$ superlattice is a three-dimensional (3D) bulk structure, while the $MASrI_3/MAPbI_3/MASrI_3$ sandwich structure has the 2D configuration with two MAI terminated surfaces. Distributions of charge-density isosurfaces in Figure S5(c) imply that the electrons and holes at CBM and VBM are both located at the region of $MAPbI_3$ in the $MAPbI_3/MASrI_3$ superlattice. Compared with the localization of surface states at VBM in the $MASrI_3/MAPbI_3/MASrI_3$ sandwich structure, the confinement of all the band-edge states at the region of $MAPbI_3$ in the $MAPbI_3/MASrI_3$ superlattice means that surfaces of perovskite thin films have a strong effect on charge distributions. As the dimension decreasing from 3D to 2D, the electrons and holes in $MAPbI_3$ thin films will distribute nonuniformly and tend to accumulate at surfaces.

This phenomenon originates from following reasons: Raman analyses have demonstrated that MA^+ molecules are more distorted in small periodic crystal, such as thin films, than those in bulk $MAPbI_3$[11, 12]. Because the MA^+ cation has a permanent dipole moment, the more randomly oriented organic molecules result in an asymmetrical electrostatic potential, which influence the distributions of electrons and holes in $MAPbI_3$ thin films. Furthermore, the effective exciton Bohr radius is ~4 nm,

and this value is almost the same as the thickness of perovskite films in this work. If the crystal is large, the permission for exciton formation (the Coulomb attraction between electrons and holes) indicates a relatively strong binding energy (from 30 to 50 meV[13-15]). While in perovskite thin films, the Coulomb attraction between electrons and holes is much weaker and electron-hole pairs are more likely to be affected by the electrostatic disorder and separate.

Section S5. The mismatch between $MAPbI_3$ and $MASrI_3$($MASrCl_3$)

According to the data listed in Table S2 to S4, we calculated lattice mismatches. The largest lattice mismatch between $MAPbI_3$ and $MASrI_3$ is within 1%, and the largest lattice mismatch between $MAPbI_3$ and $MASrCl_3$ is within 3%.

Table S2. The optimized lattice constants of $MAPbI_3$ in O- and T-phases.

Lattice Constant (Å)	$MAPbI_3$	
	orthorhombic	tetragonal
a	8.97 (8.84$^{\alpha}$, 9.04$^{\beta}$)	8.80 (8.83$^{\beta}$, 8.85$^{\gamma}$)
b	12.85 (12.58$^{\alpha}$, 12.86$^{\beta}$)	--
c	8.71 (8.56$^{\alpha}$, 8.55$^{\beta}$)	12.89 (12.98$^{\beta}$, 12.64$^{\gamma}$)

$^{\alpha}$Reference [16], the experimental data.

$^{\beta}$Reference [17], the DFT calculated data.

$^{\gamma}$Reference [5], the experimental data.

Table S3. The optimized lattice constants of $MASrI_3$ in O- and T-phases.

Lattice Constant (Å)	$MASrI_3$	
	orthorhombic	tetragonal
a	9.05 (8.99$^{\delta}$)	8.87 (8.79$^{\varepsilon}$)
b	12.96 (13.00$^{\delta}$)	--
c	8.78 (8.54$^{\delta}$)	13.01 (12.92$^{\varepsilon}$)

[δ]Reference 1, the DFT calculated data.

[ε]Reference 2, the DFT calculated data.

Table S4. The optimized lattice constants of $MASrCl_3$ in O- and T-phases.

Lattice Constant (Å)	$MASrCl_3$	
	orthorhombic	tetragonal
a	8.71	8.56
b	12.47	--
c	8.45	12.54

Section S6. The separation degree of layered *a-b-c* type MPI structures

The "separation degree" of electrons and holes by using the following equation:

$$\varepsilon_{sd} = 1 - \frac{\int_0^L min(\rho_e, \rho_h) dl}{\int_0^L max(\rho_e, \rho_h) dl} \quad \text{(S7)}$$

where ε_{sd} is the measure of "separation degree" of electrons and holes; L is the thickness of MPI structure and l is the z-coordinate perpendicular to the MPI thin film; ρ_e and ρ_h are the charge densities of electrons and holes, respectively; $min(\rho_e, \rho_h)$ and $max(\rho_e, \rho_h)$ mean the minimum and maximum values between ρ_e and ρ_h. According to eq S7, the separation degree (ε_{sd}) of electrons and holes of different layered *a-b-c* type MPI structures are listed in Table S5. It is noted that ε_{sd} values mainly concentrate at three regions. ε_{sd} of 1-2-1, 1-1-2 and 1-1-1 structures are all close to 100%, which means electrons and holes in these structures separate completely. Thus, these three structures locate at the region of the purple background. While ε_{sd} of 0-0-1,

0-0-3, 1-0-2, 0-0-2 and 1-0-1 structures are between 75% and 90% (obviously smaller than 100%), indicating that electrons and holes in these structures will partly recombine (recombination rate is less than 25%). Thus, we plotted these structures with shadowed (pink) background in Figure 4 in the revised manuscript (Figure 3 in the original manuscript). However, in the 2-0-2 structure, nearly 50% electrons and holes will recombine with each other, and its recombination rate is much larger than those in pink background (25%). Therefore, 2-0-2 structure is plotted with white background.

Table S5. The separation degree (ε_{sd}) of layered *a-b-c* type MPI structures with different Sr-Cl intercalation layers.

a-b-c type	ε_{sd} (%)
1-2-1	99.98
1-1-2	99.66
1-1-1	99.42
0-0-1	85.27
0-0-3	85.17
1-0-2	82.26
0-0-2	79.71
1-0-1	75.32
2-0-2	58.12

Section S7. Optical absorption spectra of perovskites with {100} surfaces

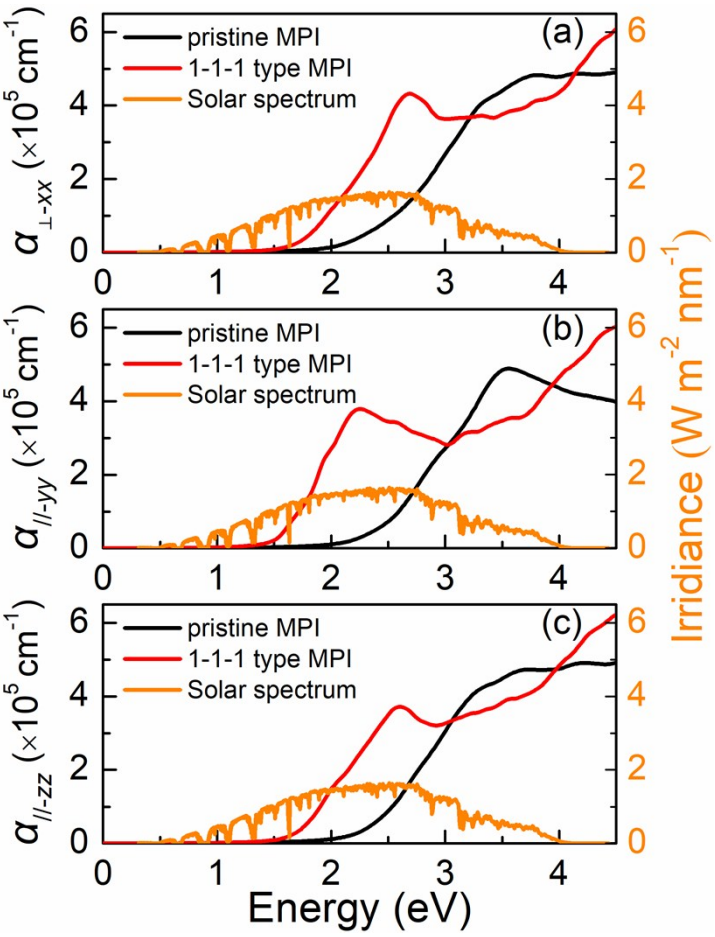

Figure S6. Optical absorption spectra of {100} faceted pristine MPI and 1-1-1 type MPI thin films along (a) out-of-plane ($\alpha_{\perp\text{-}xx}$), (b) *y* in-plane ($\alpha_{//\text{-}yy}$) and (c) *z* in-plane ($\alpha_{//\text{-}zz}$) polarization directions. The solar spectrum is plotted in the right-Y coordinate as a reference.

Section S8. Projected density of states of pristine MPI and 1-1-1 type MPI structure

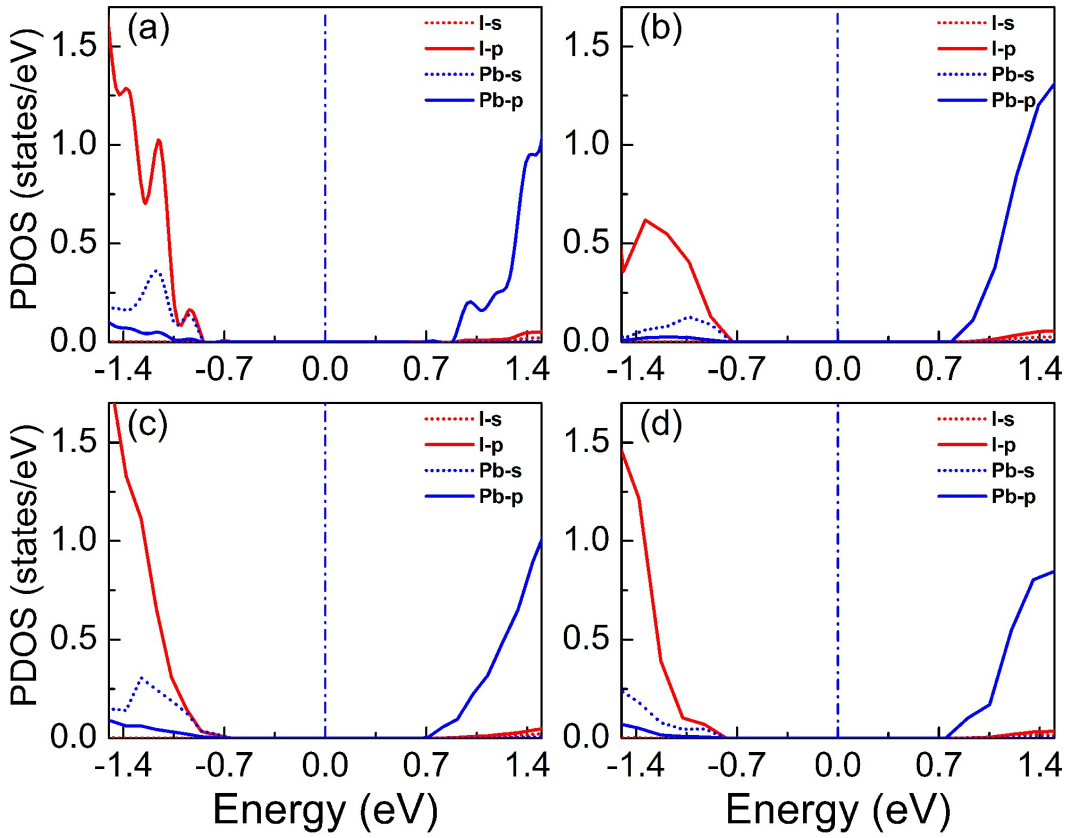

Figure S7. The projected density of states of (a) pristine MPI with {100} surfaces, (b) 1-1-1 type MPI with {100} surfaces, (c) pristine MPI with {110} surfaces and (d) 1-1-1 type MPI with {110} surfaces. The position of Fermi level is set to energy zero.

Section S9. Fictitious cleavage surfaces of 1-1-1 type MPI structure

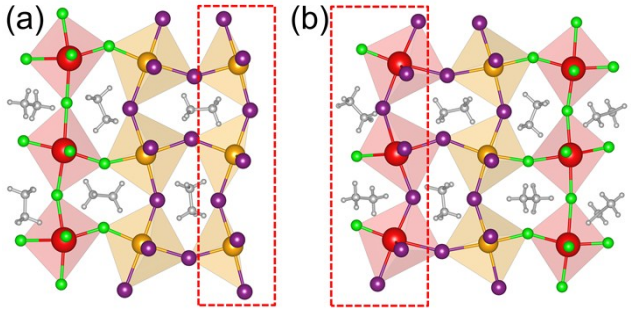

Figure S8. Crystal structures of (a) three-layered exfoliation and (b) three-layered cleaved structure. Structures emphasized in red boxes in Figures (a) and (b) are Pb-I and Sr-Cl cleavage surfaces, respectively.

Because extra Sr-Cl-layers are inserted into $MAPbI_3$, interfaces between Sr-Cl-layer and Pb-I-layer are introduced into *a-b-c* type MPI structure, which may result in instability at these interfaces. If an interface is cleaved, it leaves two surfaces exposed,

that is the Pb-I and Sr-Cl surfaces. In order to investigate the cleavage energy of the interface between Sr-Cl-layer and Pb-I-layer in the 1-1-1 type layered structure, we fictitiously cleaved the six layers of 1-1-1 type MPI into two parts: one part is an exfoliation with a Pb-I surface and the other part is a cleaved structure with a Sr-Cl surface, as shown in Figures S8(a) and (b), respectively. Each part has three layers. This cleavage surface is along the interface between Sr-Cl-layer and Pb-I-layer.

Section S10. The decomposition enthalpies of 1-1-1 type MPI structure

According to the decomposition reaction of $MAPbI_3$[18], two extreme decomposition pathways of the 1-1-1 type layered structure are considered:

$$MA_{n+1}Pb_{0.5n}Sr_{0.5n}I_{1.5n+1}Cl_{1.5n} \rightarrow n/2\ PbI_2 + n/2\ SrCl_2 + (n/2+1)\ MAI + n/2\ MACl \quad (S8)$$

$$MA_{n+1}Pb_{0.5n}Sr_{0.5n}I_{1.5n+1}Cl_{1.5n} \rightarrow n/2\ PbCl_2 + n/2\ SrI_2 + (n/2+1)\ MAI + n/2\ MACl \quad (S9)$$

All the other decomposition pathways are between these two extreme ones. Table S6 exhibits the two decomposition pathways and the associated decomposition enthalpies (ΔH_d). It can be found that the decomposition enthalpy of either decomposition pathway is positive, which means an endothermic reaction.

Table S6. The decomposition pathways and the associated decomposition enthalpies (ΔH_d) of the layered 1-1-1 type layered structure.

Decomposition Pathway	**ΔH_d (meV/atom)**
PbI_2+$SrCl_2$+MA+HI+HCl	1.797
$PbCl_2$+SrI_2+MA+HI+HCl	23.969

Section S11. The stability of different surface defects

To study the stability of surface defects of perovskite, eight types of point defects

are considered, including of an additional I(Cl) atom ($I_i(Cl_i)$), an I(Cl) atom substituting a MA molecule ($I_{MA}(Cl_{MA})$), an I(Cl) atom vacancy ($V_I(V_{Cl})$), a MA molecule vacancy (V_{MA}), an additional Pb(Sr) atom ($Pb_i(Sr_i)$), a Pb(Sr) atom substituting an I(Cl) atom ($Pb_{I(Cl)}(Sr_{I(Cl)})$), a Pb(Sr) atom substituting a MA molecule ($Pb_{MA}(Sr_{MA})$) and a Pb(Sr) atom vacancy ($V_{Pb}(V_{Sr})$).

The stability of various surface defects is evaluated by their formation energies (E_f), which are calculated as follows:

$$E_f = E_D - (E_T + \Delta E_T) + \Delta n_i \sum_i E_i \quad \text{(S10)}$$

where E_D is the total energy of a specific terminated surface with a surface defect. E_i is the average energy of one atom in bulk (i = Pb(Sr) or I(Cl)) or the energy of one MA molecule. Δn_i is the difference of the number of Pb(Sr) atoms, I(Cl) atoms and MA molecules between perovskite surfaces with and without defects.

Table S7. The calculated formation energies of various defects in $MAPbI_3$ facets with vacant termination.

Formation Energy (eV)	**{100} facet**	**{110} facet**
I_i	0.193	0.2511
I_{MA}	3.801	3.654
V_I	2.076	2.150
V_{MA}	4.276	4.253
Pb_i	1.027	1.276
Pb_I	3.361	3.353
Pb_{MA}	3.831	3.623
V_{Pb}	3.014	2.317

Table S8. The calculated formation energies of various defects in $MAPbI_3$ facets with flat termination.

Formation	**{100}**	**{110}**

Energy (eV)	facet	facet
I_i	0.557	1.078
V_I	2.038	4.466
Pb_i	1.183	1.969
Pb_I	3.500	5.347
V_{Pb}	3.187	7.029

Table S9. The calculated formation energies of various defects in $MAPbI_3$ facets with MAI termination.

Formation Energy (eV)	{100} facet	{110} facet
I_i	0.112	1.300
I_{MA}	3.645	4.826
V_I	2.578	4.321
V_{MA}	3.906	5.159
Pb_i	2.132	2.226
Pb_I	3.240	5.445
Pb_{MA}	3.998	3.208
V_{Pb}	3.040	6.614

Table S10. The calculated formation energies of various defects in $MASrI_3$ facets with vacant termination.

Formation Energy (eV)	{100} facet	{110} facet
I_i	0.390	0.657
I_{MA}	3.615	4.139
V_I	3.655	3.883
V_{MA}	4.506	4.955
Sr_i	1.463	1.804

Sr_I	4.551	4.558
Sr_{MA}	1.952	2.223
V_{Sr}	4.902	5.383

Table S11. The calculated formation energies of various defects in $MASrI_3$ facets with flat termination.

Formation Energy (eV)	**{100} facet**	**{110} facet**
I_i	1.545	1.078
V_I	4.893	4.466
Sr_i	2.508	1.969
Sr_I	5.566	5.347
V_{Sr}	7.308	7.029

Table S12. The calculated formation energies of various defects in $MASrI_3$ facets with MAI termination.

Formation Energy (eV)	**{100} facet**	**{110} Facet**
I_i	0.112	1.300
I_{MA}	3.383	4.826
V_I	3.559	4.321
V_{MA}	4.057	5.159
Sr_i	1.093	2.226
Sr_I	4.048	5.445
Sr_{MA}	2.165	3.208
V_{Sr}	4.067	6.614

Table S13. The calculated formation energies of various defects in $MASrCl_3$ facets with vacant termination.

Formation Energy (eV)	{100} facet	{110} facet
Cl_i	0.273	0.208
Cl_{MA}	5.086	4.775
V_{Cl}	4.100	3.952
V_{MA}	5.293	5.315
Sr_i	0.974	0.867
Sr_{Cl}	5.293	4.509
Sr_{MA}	1.513	0.989
V_{Sr}	7.541	6.705

Table S14. The calculated formation energies of various defects in $MASrCl_3$ facets with flat termination.

Formation Energy (eV)	{100} facet	{110} facet
Cl_i	0.203	0.433
V_{Cl}	4.105	4.224
Sr_i	0.609	1.041
Sr_{Cl}	4.787	4.456
V_{Sr}	8.406	7.083

Table S15. The calculated formation energies of various defects in $MASrCl_3$ facets with MACl termination.

Formation Energy (eV)	{100} facet	{110} facet
Cl_i	0.100	0.630
Cl_{MA}	4.241	4.955
V_{Cl}	3.847	4.100
V_{MA}	5.028	5.388

Sr_i	0.365	1.209
Sr_{Cl}	4.609	5.356
Sr_{MA}	1.382	1.841
V_{Sr}	7.778	8.016

REFERENCES

1. S. Pramchu, Y. Laosiritaworn and A. Punya Jaroenjittichai, *Integrated Ferroelectrics*, 2016, **175**, 193-201.
2. X. Zhu, H. Su, R. A. Marcus and M. E. Michel-Beyerle, *The Journal of Physical Chemistry Letters*, 2014, **5**, 3061-3065.
3. F. Zheng, H. Takenaka, F. Wang, N. Z. Koocher and A. M. Rappe, *The Journal of Physical Chemistry Letters*, 2014, **6**, 31-37.
4. P. Umari, E. Mosconi and F. De Angelis, *Scientific Reports*, 2014, **4**, 4467.
5. C. C. Stoumpos, C. D. Malliakas and M. G. Kanatzidis, *Inorganic Chemistry*, 2013, **52**, 9019-9038.
6. S. Pramchu, Y. Laosiritaworn and A. P. Jaroenjittichai, *Integrated Ferroelectrics*, 2016, **175**, 193-201.
7. M. Pazoki, T. J. Jacobsson, A. Hagfeldt, G. Boschloo and T. Edvinsson, *Physical Review B*, 2016, **93**, 144105.
8. T. J. Jacobsson, M. Pazoki, A. Hagfeldt and T. Edvinsson, *The Journal of Physical Chemistry C*, 2015, **119**, 25673-25683.
9. H. Zhang, J. Mao, H. He, D. Zhang, H. L. Zhu, F. Xie, K. S. Wong, M. Grätzel and W. C. Choy, *Advanced Energy Materials*, 2015, **5**, 1501354.
10. G.-X. Liang, P. Fan, D. Gu, Z.-H. Zheng, D.-P. Zhang, J.-T. Luo, X.-H. Zhang and H.-L. Ma, *IEEE Journal of Photovoltaics*, 2016, **6**, 1537-1541.
11. G. Grancini, S. Marras, M. Prato, C. Giannini, C. Quarti, F. De Angelis, M. De Bastiani, G. E. Eperon, H. J. Snaith and L. Manna, *The Journal of Physical Chemistry Letters*, 2014, **5**, 3836-3842.
12. C. Quarti, G. Grancini, E. Mosconi, P. Bruno, J. M. Ball, M. M. Lee, H. J. Snaith, A. Petrozza and F. De Angelis, *The Journal of Physical Chemistry Letters*, 2013, **5**, 279-284.
13. N. Sestu, M. Cadelano, V. Sarritzu, F. Chen, D. Marongiu, R. Piras, M. Mainas, F. Quochi, M. Saba and A. Mura, *The Journal of Physical Chemistry Letters*, 2015, **6**, 4566-4572.
14. K. Tanaka, T. Takahashi, T. Ban, T. Kondo, K. Uchida and N. Miura, *Solid State Communications*, 2003, **127**, 619-623.
15. T. Ishihara, *Journal of Luminescence*, 1994, **60**, 269-274.
16. T. Baikie, Y. Fang, J. M. Kadro, M. Schreyer, F. Wei, S. G. Mhaisalkar, M. Graetzel and T. J. White, *Journal of Materials Chemistry A*, 2013, **1**, 5628-5641.
17. H. Zhu and J.-M. Liu, *Scientific Reports*, 2016, **6**, 37425.

18. J. H. Heo, D. H. Song, H. J. Han, S. Y. Kim, J. H. Kim, D. Kim, H. W. Shin, T. K. Ahn, C. Wolf and T. W. Lee, *Advanced Materials*, 2015, **27**, 3464.